Characterization of the Kinematics of the Cordillera Blanca Normal Fault from InSAR

Sylvain Michel[1,2] , Léa Pousse-Beltran[3], Laurence Audin[3], Juan Carlos Villegas Lanza[4], Marie-Pierre Doin[3], Bertrand Lovery[3], Swann Zerathe[3], Mohamed Chlieh[3]

[1] Université Côte d'Azur, CNRS, IRD, Observatoire de la Côte d'Azur, Géoazur, Sophia-Antipolis, France

[2] CNRS-INSU, Institut des Sciences de la Terre Paris, Sorbonne Université, ISTeP UMR 7193, 75005 Paris, France

[3] Université Grenoble Alpes, Université Savoie Mont Blanc, CNRS, IRD, Université Gustave Eiffel, ISTerre, 38000 Grenoble, France.

[4] Instituto Geofísico del Perú, Lima, Peru

Sylvain Michel (sylvain.michel@geoazur.unice.fr)
Léa Pousse-Beltran (lea.pousse@univ-grenoble-alpes.fr)
Laurence Audin (laurence.audin@ird.fr)
Juan Carlos Villegas Lanza (jvillegas@igp.gob.pe)
Marie-Pierre Doin (marie-pierre.doin@univ-grenoble-alpes.fr)
Bertrand Lovery (bertrand.lovery@univ-grenoble-alpes.fr)
Swann Zerathe (swann.zerathe@ird.fr)
Mohamed Chlieh (mohamed.chlieh@univ-grenoble-alpes.fr)

The manuscript is a non-peer reviewed preprint submitted to EarthArXiv

Abstract

The Cordillera Blanca Normal fault (CBNF), located along the western margin of the Cordillera Blanca batholith in northern Peru, is a major extensional structure of the central Andes. Geological and geomorphological evidence indicates sustained slip over the past ~4 Ma, yet its present-day kinematics have not been quantified geodetically. Here, we use Sentinel-1 InSAR (Interferometric synthetic-aperture radar) data acquired between 2015 and 2021 to provide the first geodetic characterization CNBF. Fault-perpendicular line-of-sight (LOS) velocity profiles were extracted at regular intervals along the ~150 km-long fault and modeled using a Bayesian framework to explore a wide range of kinematic scenarios and associated uncertainties. Assuming a freely creeping fault, we infer a slip rate of ~2-2.5 mm/yr along the well-defined central segment of the mapped trace, consistent with independent geological and geomorphological estimates. When left unconstrained, fault dip and rake remain poorly resolved due to the limited signal-to-noise ratio to the InSAR data. However, imposing a purely dip-slip mechanism, in agreement with geological observations, significantly tightens parameter uncertainty and reveals a northward decrease in dip from ~45° to ~20° in the central segment. Southward, deformation appears more diffuse and model parameters less constrained, reflecting distributed strain and structural complexity. Although current uncertainties (~0.7 mm/yr) limit our ability to robustly assess fault locking, our results establish a first quantitative geodetic picture of the CNBF kinematics. Those constraints can be further refined in future work through longer InSAR time series and complementary GNSS observations, enabling a more reliable evaluation of the fault's seismogenic potential.

1. Introduction

The Cordillera Blanca in the Peruvian Andes reaches elevations above 6,000 m and is composed of an ∼8 Ma batholith (McNulty et al., 1998). This batholith represents the final magmatic episode in northern Peru, which has ceased following the onset of the flattening of the subduction slab. It trends parallel to the overall Andean range and the coast (located ∼100 km to the west), extends ∼200 km in length, is ∼20 km wide, and plunges southward (Cobbing et al., 1981). The internal fabric of the batholith suggests that it intruded along a pre-existing lithospheric fault structure during a period dominated by strike-slip tectonics (Cobbing et al., 1981; McNulty et al., 1998; Petford & Atherton, 1992). Since its formation, the Cordillera Blanca has experienced multiple changes of tectonic regimes and is currently undergoing extension (Margirier et al., 2017).

The batholith is bounded to its west by the Cordillera Blanca normal fault (CBNF), which dips ∼40°W (Margirier et al., 2017). The fault is well defined in its northern portion, between 8.5°S and 9.5°S, but becomes more diffuse to the south, where it forms an en echelon fault system (Giovanni, 2007). Thermochronologic data indicate exhumation rates of ∼2 mm/yr and >1 mm/yr over the last 3 Ma for the central section of the CBNF, as estimated by Giovanni (2007) and (Hodson, 2013), respectively, with rates decreasing toward the south. In contrast, (Margirier et al., 2016) estimated a lower exhumation rate of ∼1 mm/yr for the central section over the last 4 Ma based on the same techniques. Based on geomorphological evidence, (Bonnot, 1984) inferred an exhumation rate of ∼0.7 mm/yr over the last 3 Ma. Finally, using geomorphological markers and combined with ^{10}Be dating, vertical slip rates over the last ∼30 ka have been estimated to range from 0.7-3.0 mm/yr in the northern CBNF to 0.9-1.4 mm/yr in the south (Schwartz, 1988; Siame et al., 2006) .

No major historical earthquakes (M>6) have been documented directly on the CBNF. However, microseismicity recorded in its vicinity shows focal mechanisms consistent with the regional NE-SW extensional stress regime (Deverchère et al., 1989; Margirier et al., 2017). At the regional scale, several significant earthquakes have affected the Cordillera Blanca area. In particular, a Mw 6.8 occurred in 1946 on the Quiches normal fault, located ∼50 km northeast from the CBNF (Bellier et al., 1991; Doser, 1987). The most important seismic event in the region was the 1970 Mw 7.9 Ancash earthquake, located within the subducting slab slightly offshore in front of the CBNF. This event exhibited a normal-faulting mechanism and triggered landslides and a debris avalanche in the Cordillera Blanca, resulting in approximately 70,000 casualties (Cluff, 1971). Within four years following this earthquake, five additional events with magnitudes between Mw 5 and 6 occurred within 30km of the CNBF at depths lower than 40 km (U.S. Geological Survey, 2017). With the same magnitude and location criteria, only four comparable seismic events have been recorded since 1916 (U.S. Geological Survey, 2017).

Although no large earthquakes have been documented on the CBNF, it remains unclear whether the fault is currently accumulating elastic strain that could be released in a future seismic event. Moreover, estimates of the fault's exhumation rate are based exclusively on methods that integrate deformation over geological timescales (>30 ka). To date, the present-day tectonic regime and kinematics of the CBNF have not been documented using geodetic observations. The aim of this study is therefore to provide the first geodetic characterization of the CBNF kinematics based on InSAR data. First, we present the datasets used in this study, followed by a description of the Bayesian approach to estimate the fault kinematics. We then present and discuss the results, including the limitations of the approach, before concluding.

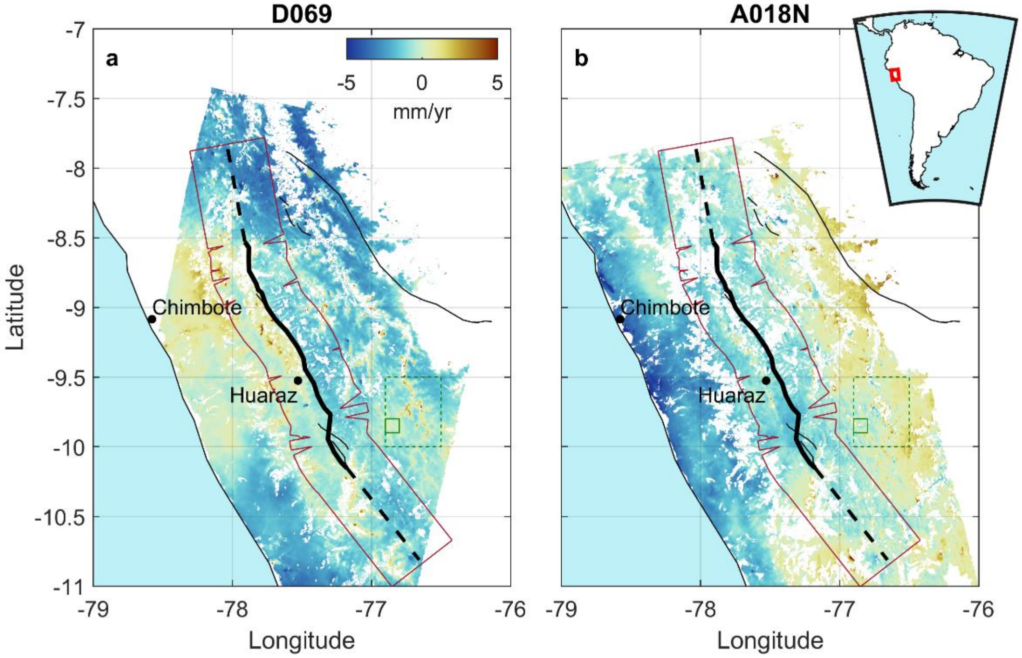

Figure 1: Regional setting of the Cordillera Blanca and InSAR (Interferometric synthetic-aperture radar) velocity maps. (a) Descending track D016 velocity map. (a) Ascending track A018N velocity map. Thin black solid lines indicate mapped fault traces (Costa et al., 2016, 2020), while the thick black solid line marks the Cordillera Blanca Normal Fault considered in this study. The thick black dashed lines represent arbitrary lateral extensions of the mapped fault trace. The red contour delineates the profile locations. The solid green square indicates the spatial reference area used to produce the velocity maps, and the dashed green square marks the area used to estimate the uncertainty of the velocity field. The inset on the right shows the location of the study area within South America.

2. Data

The free Sentinel-1 SAR image archive enables large-scale monitoring of ground deformation over a decade (e.g., Lemrabet et al., 2023). The InSAR time series over the region of interest were generated using the FormaTerre LArge-Scale Multi-Temporal Sentinel-1 InterferoMetry (FLATSIM) service (FormaTerre, 2020; Thollard et al., 2021), operated by the French Centre National d'Études Spatiales (CNES). The processing relies on the New Small Baseline (NSBAS) approach (Doin et al., 2011; Grandin, 2015) and includes a correction of atmospheric propagation delays for each interferogram, based on global atmospheric models, using the ERA5 meteorological analysis from the European Centre for Medium-Range Weather Forecasts (ECMWF) (e.g., Jolivet et al., 2011). We two orbital tracks were analyzed (Fig. 1): the ascending A018 track, covering a period between 2015-01-10 to 2021-04-26, with 141 dates used to generate 675 interferograms; and the descending D069 track, covering a period between 2015-01-02 to 2021-04-30, with 134 dates used to generate 616 interferograms. To correct possible effect of remaining topographic contribution, we removed a linear trend to the mean velocity map estimated by fitting the phase versus the topography excluding the Cordillera Blanca.

The data is further cleaned following a multi-step procedure. For both tracks D069 and A018N, we remove all data points with a root-mean-square (RMS) value greater than 0.2. In addition, we discarded pixels with a proxy of the temporal coherence of the interferograms' stack lower than 28 for track D069 and 26 for track A018N in order to mask glacier areas. The InSAR velocity fields are then spatially referenced using the area outlined by the green solid square in Fig. 1. This reference zone lies outside the main area of interest but is sufficiently close to ensure spatial continuity of the deformation signal within the study area. Finally, we exclude areas previously identified as landslides (Klimeš et al., 2025). These masked zones are limited to the region in the immediate vicinity of the CBNF. Landslides located outside this restricted zone but still within the broader area of interest were not removed and therefore remain in the dataset, contributing to the overall noise.

3. Method

To characterize the kinematics of the CBNF, we extract fault-perpendicular line-of-sight (LOS) deformation rate profiles at 3.8 km intervals along the fault and test a simple kinematic model that describes surface deformation rate associated with a freely creeping fault, assuming no locked portion at the fault's interface. Under these assumptions, the model predicts a step function in surface deformation rate across the fault trace.

Because the fault trace has been documented primarily through geological observations (Costa et al., 2016, 2020), we laterally extend the fault beyond its mapped extent, as shown in Fig. 1, to account for the possibility that it continues beyond the currently documented sections.

Each deformation rate profile is 60 km long (i.e. 30 km on either side of the fault). InSAR data located within a perpendicular distance of 3.8 km from each fault-perpendicular profile are assigned to that profile. Each profile is further subdivided into 1 km-long sections, to which the corresponding InSAR observations are aggregated. In total, a 100 profiles are extracted, each divided into 60 sections.

For each profile section, we compute the variance of the assigned data. However, this variance is considered to underestimate the total observational uncertainty. To account for additional noise sources, we add a supplementary variance term, calculated separately for each InSAR track from a reference area located between 76.9°W and 76.5°W longitude and between 10°S and 9.5°S latitude. This area lies within the Andean range but shows no clear evidence of localized deformation and is therefore assumed to represent background noise.

The predicted LOS displacement rates of the model, $\dot{D}_{A018N}$ and $\dot{D}_{D069}$ for tracks A018N and D069, respectively, are defined by seven parameters: (1) the position of the fault relative to a reference location given by the mapped fault trace, P; (2) the fault slip-rate amplitude, V; (3) the slip rake (negative for normal slip), λ; (4) the fault strike, ϕ; (5) the fault dip, δ; and (6-7) the constants C_{A018N} and C_{D069}, which represent constant offsets of the deformation rate profiles for tracks A018N and D069, respectively.

The modeled deformation profiles are expressed as:

$$\dot{D}_{A018N} = \left[\left(V\boldsymbol{v}\left(H(X-P)-\frac{1}{2}\right)\right)\cdot \boldsymbol{a}_{A018N}\right] + C_{A018N}$$
$$\dot{D}_{D069} = \left[\left(V\boldsymbol{v}\left(H(X-P)-\frac{1}{2}\right)\right)\cdot \boldsymbol{a}_{D069}\right] + C_{D069},$$

where $\overline{\boldsymbol{a}}_{A018N}$ and $\overline{\boldsymbol{a}}_{D069}$ are the unit LOS direction vectors for tracks A018N and D069, respectively, (positive values indicate motion away from the satellite), and $\boldsymbol{v}$ is the unit slip-direction vector. The components of $\boldsymbol{v}$ are given by:
$v_x = \cos(\lambda)\sin(\phi) - \sin(\lambda)\cos(\delta)\cos(\phi),$
$v_y = \cos(\lambda)\cos(\phi) + \sin(\lambda)\cos(\delta)\sin(\phi),$
$v_z = -\sin(\lambda)\sin(\delta).$

Here, H denotes the Heaviside step function, and $\cdot$ represents the dot product. X corresponds to the fault perpendicular distance. The parameter P accounts for a possible offset between the mapped fault trace and the effective location of deformation inferred from the data. This offset may result from uncertainties in the mapped fault position, from a non-vertical fault dip combined with the presence of locked areas along the faults interface, or from a listric fault geometry that shifts the surface expression of deformation away from the mapped trace.

Because the expected fault slip rates are small (~0-3 mm/yr based on geological estimates; Schwartz, 1988; Siame et al., 2006) relative to the estimated InSAR uncertainties (~0.6-0.7 mm/yr standard deviation), and given both the simplicity of the model and the fact that the fault has previously been studied only using geological approaches, we explore the parameter space using a Markov Chain Monte Carlo (MCMC) approach (Hasting, 1970; Metropolis et al., 1953). This strategy, described below, allows us to consider a broad range of plausible kinematic scenarios.

The fault strike ϕ is fixed based on the mapped fault trace, while all other parameters are allowed to vary. Uniform prior distributions are assigned to all free parameters: $\mathcal{U}$(-30,30) km for the fault position offset P; $\mathcal{U}$(0,10) mm/yr for the slip rate amplitude V; $\mathcal{U}$(0,180)° for the rake λ; $\mathcal{U}$(0,90)° for the dip δ, constraining the fault to westward dipping geometries; and $\mathcal{U}$(-3,3) mm/yr for the offset terms C_{A018N} and C_{D069}.

We sample the parameter space using 15,000 MCMC iterations and discard the first 1,000 samples as burn-in to remove the initial convergence phase of the algorithm. The posterior parameter distributions are approximated from the MCMC samples by discretizing the parameter space into bins. For each bin, the number of samples it contains divided by the total number of retained samples provides an estimate of the posterior probability mass. The bin sizes are defined as follows: P is discretized using bins of 0.6 km, V using bins of 0.2 mm/yr, λ using bins of 1.8°, δ using bins of 0.9°, and C_{A018N} and C_{D069} using bins of 0.6 mm/yr. The results are presented in the following section.

4. Results

The results are presented in Figs. 2 and 3.

The MCMC-derived fault position relative to the mapped fault trace (i.e., the parameter P) is shown in Fig. 2a-c. Between latitude 9.5°S and 8.8°S, the posterior distribution of P is relatively well constrained near 0 km (Fig. 2c), corresponding to the mapped fault position, where the fault trace is clearly defined (see Introduction). In contrast, along the remainder of the fault within the initially mapped area (delimited by the red bars in Fig. 2c), the distribution of P is broader, consistent with more diffuse deformation expected in the southern portion of the CBNF (south of 9.5°S; see Introduction). Outside the initially mapped fault extent, P is locally constrained in some sections, although those sections are spatially discontinuous.

The black dots in Fig. 2a and b represent the mean value of P from the posterior distribution for each profile and allow direct comparison with the LOS deformation rate profiles. For track D069, the mean P coincides with the location of a strong deformation rate gradient between latitude 9.5°S and 8.8°S (Fig. 2a), and becomes increasingly scattered southward between 10.1°S and 9.5°S, consistent with the more distributed deformation in this region. For track A018N, the deformation rate contrast across the mapped fault is more subtle, and the location of P is therefore less well constrained by this track alone. Nevertheless, this weak signal provides in itself an information when combined with track D069. For instance, if the fault accommodates normal slip and dips westward, as suggested by geological observations, this subdued LOS signal on track A018N can be explained by the combination of westward motion (toward the satellite) and subsidence (away from the satellite) on the western side of the fault. The superposition of these opposing components would reduce the net LOS displacement rate, leading to a weaker observable signal.

The posterior slip rate distributions (Fig. 2g) are relatively consistent along the fault, with peak probability values on the order of ~ -2.5 mm/yr (negative values corresponding to a normal-slip mechanism). At some locations, higher slip rates exceeding 5 mm/yr are permitted by the posterior distribution but remain of low probability (e.g. profile at latitude 9.45°S). At a few isolated locations, positive slip rates (i.e. thrust) are observed; however, these cases are generally associated with markedly different inferred fault positions and near strike slip kinematics (e.g. profiles at latitude 11.8°S, 10.2°S and 8.4°S).

The posterior dip distributions for profiles between latitude 9.5°S and 8.8°S, corresponding to the well-defined portion of the fault, indicate that dip angles are generally poorly constrained but exhibit a lower bound of the probability distribution at ~40° in the south of this segment gradually decreasing northward to ~0°. North of the well-defined fault section (north of 8.8°S), the dip distributions are comparatively better constrained, with inferred dips raging between ~25° and ~50°. South of the well-defined fault section (south of 9.5°S), the posterior dip distribution are nearly uniform between ~30° and ~90° dip, indicating little constraint on fault dip in this region.

Finally, the posterior rake distributions are very poorly constrained, exhibiting uniform probability between 0° and 150°. Only a few localized sections of the fault show more constrained rake distributions, centered around ~150°, and these occur outside the well-defined portion of the fault.

Although several parameters exhibit large uncertainties, correlations exist between some of them, as illustrated in Fig. 3a-c for the profile located at latitude 9.3°S. For this profile, the most pronounced tradeoff occurs between slip rate and rake (Fig. 3a). The inferred slip rate depends strongly on the rake value, reaching a minimum near a rake of 65° and increasing as the rake deviates from this value. Note that constraining the rake to values close to 90°, as suggested by geological observations for the central portion of the CNBF, would also substantially restrict the inferred dip to values around ∼35° (Fig. 3b).

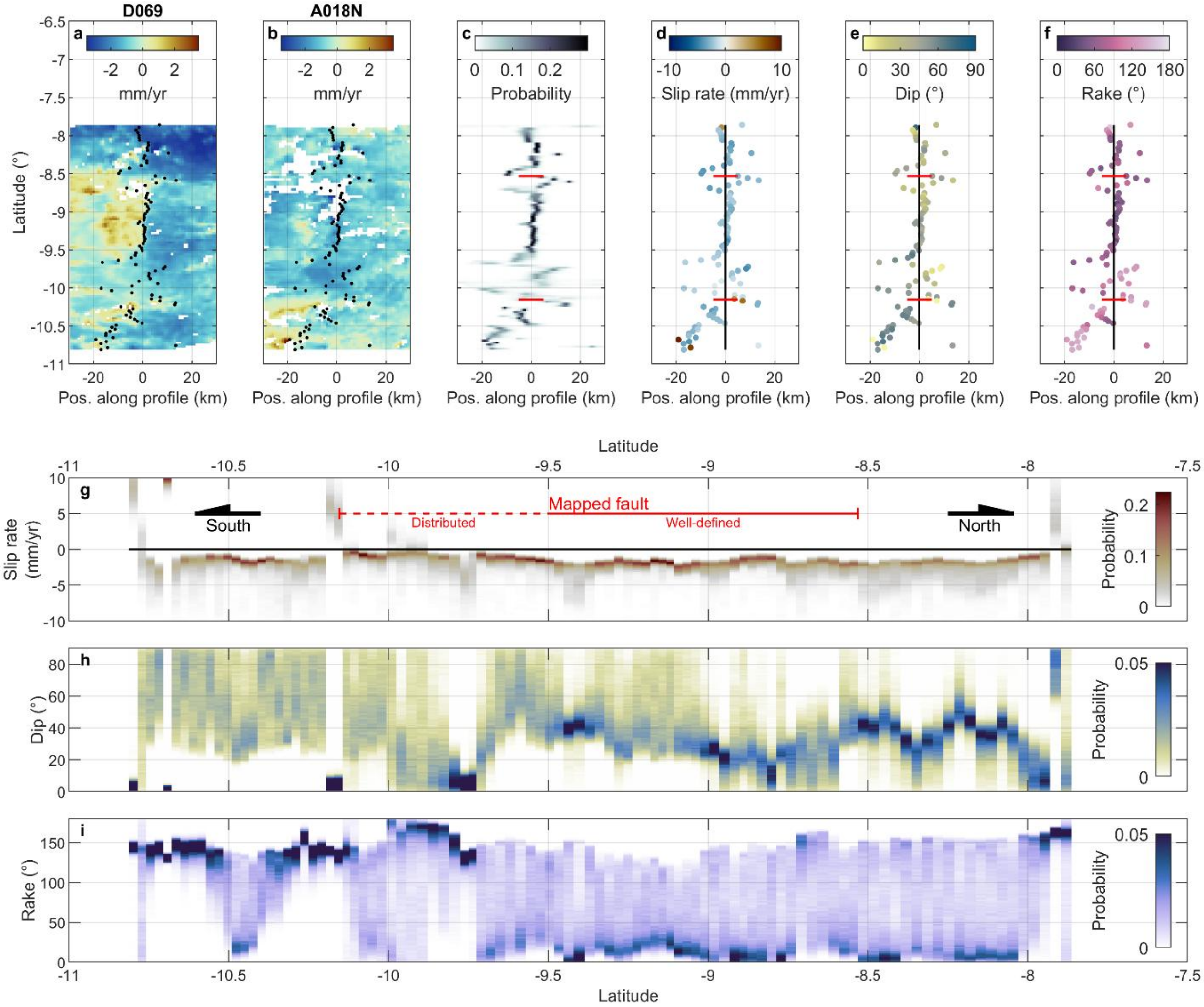

Figure 2: Results of the MCMC analysis of the kinematics of the Cordillera Blanca Normal Fault. (a) Velocity profiles from track A018N. Black dots represent the mean value of P for each profile, corresponding to the inferred fault position relative to a reference defined by the mapped fault trace. (b) Same as (a), but for track D069. (c) Posterior probability distribution of P. The horizontal red bars indicate the extent of the mapped fault trace. Panels (d), (e) and (f) show the mean value of P for each profile, with color indicating the mean slip rate (V), mean dip (δ), and mean rake (λ), respectively. Panels (g), (h) and (i) present the posterior probability distributions of V, δ, and λ, respectively.

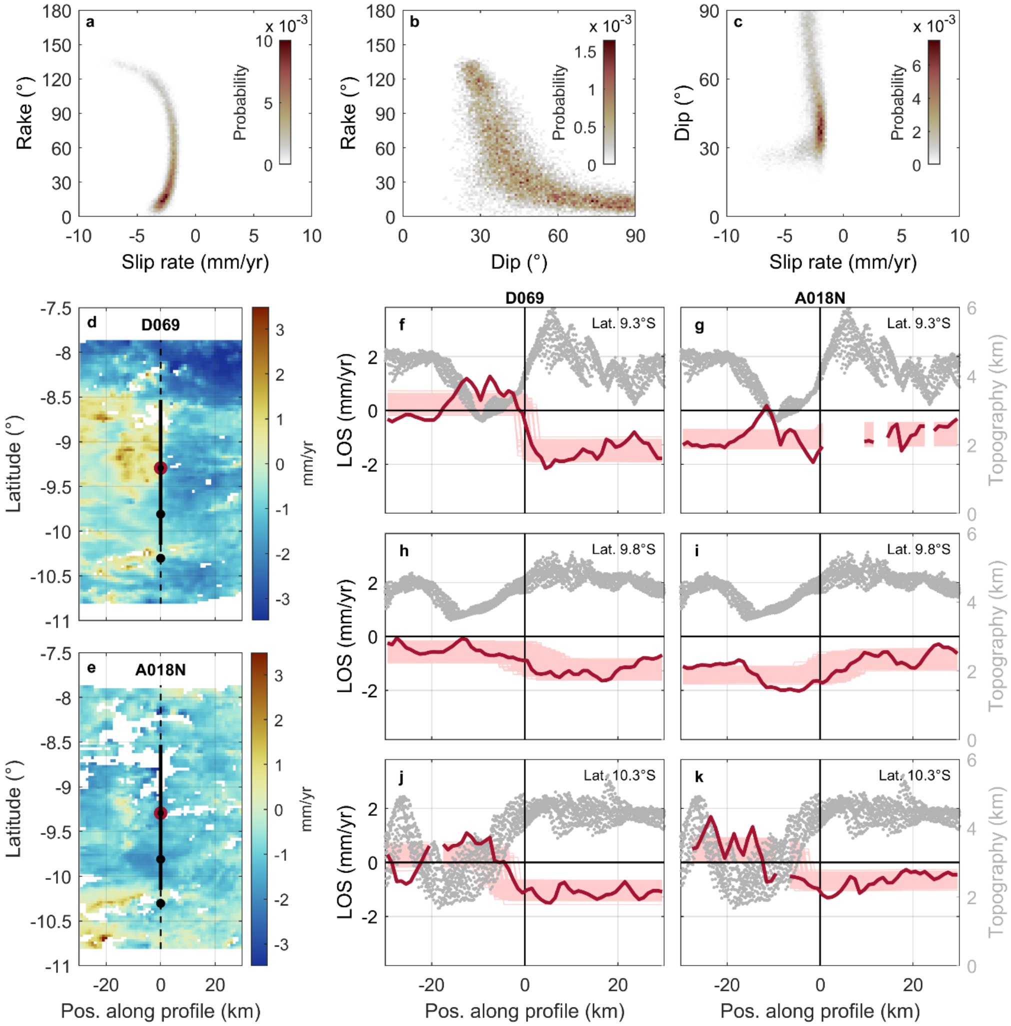

Figure 3: Parameter correlations and model fit to the data. Panels (a-c) show the correlations between slip rate, dip and rake for the profile marked by the red dot in panels (d) and (e). Panels (d) and (e) display the LOS velocity profiles for tracks D069 and A018N, respectively. Panels (f-k) compare the observed LOS velocity profiles — which locations are indicated by the black and red dots in panels (d) and (e) — with model predictions derived from 1,500 MCMC samples (pink curves), together with the corresponding topography profiles (gray dots). The left column corresponds to track D069, and the right column corresponds to A018N.

5. Discussion

The results presented in the previous section indicate slip rate of ~2 mm/yr along the central section of the CBNF. However, several limitations related to both the modeling approach and data processing must be considered.

First, the model accounts for only a single fault, whereas multiple faults may be present within the profiles. In particular, structures potentially associated with the Cordillera Negra could also accommodate significant slip. The current model therefore represents a simplification of the tectonic setting. Moreover, the strike parameter was not explored, although it could influence the results—especially in areas where deformation is spatially distributed and the uncertainty in fault trace location and orientation is high.

Second, the region's pronounced topography—reaching 6,768 m for Huascarán, the highest peaks—may introduce residual topographic artifacts in the InSAR velocity field. Although LOS uncertainties were estimated in mountainous terrain and should at least partially account for this type of error, some topographic effects may still persist. Nevertheless, in the central section of the CBNF, the sharp gradient in LOS displacement rate occurs along the continuous slope toward the Cordillera Blanca range rather than at the valley floor, suggesting a tectonic origin for the signal. In contrast, several profiles south of the mapped CBNF trace appear to show LOS signals that are anticorrelated with topography. These results should therefore be interpreted with caution.

The inversion was performed using conservative priors, particularly for dip and rake, in order to provide an evaluation of the CBNF kinematics independent of the geological observations. However, when incorporating geological evidence indicating that the fault rake is close to a purely normal mechanism (e.g., a Gaussian prior centered at 90° with a standard deviation of 10°), as suggested for the central section of the CBNF (Bonnot, 1984; Margirier et al., 2017), the model parameters become more tightly constrained (Fig. 4). In this case, the decrease in dip along the well-defined fault section, from ∼45° in the south to ∼20° in the north, becomes much clearer.

Nevertheless, our results rely on an observational uncertainty estimated from a specific reference area, which may lead to an underestimation of the true uncertainty. In addition, methodological uncertainties are not included in this estimate. To illustrate the impact of the assumed uncertainty on the inversion results, Fig. 5 presents the results for a fault with a normal mechanism (similarly to Fig.4), but using observational uncertainties that are twice as large. The overall results remain consistent with those shown in Fig. 4, although the posterior parameter distributions are broader. However, within the distributed-deformation section of the fault, the posterior distributions become very wide, approaching the uniform prior distribution. This behavior likely reflects the diffuse nature of the deformation in this section and highlights the limitations of the model in capturing such distributed deformation.

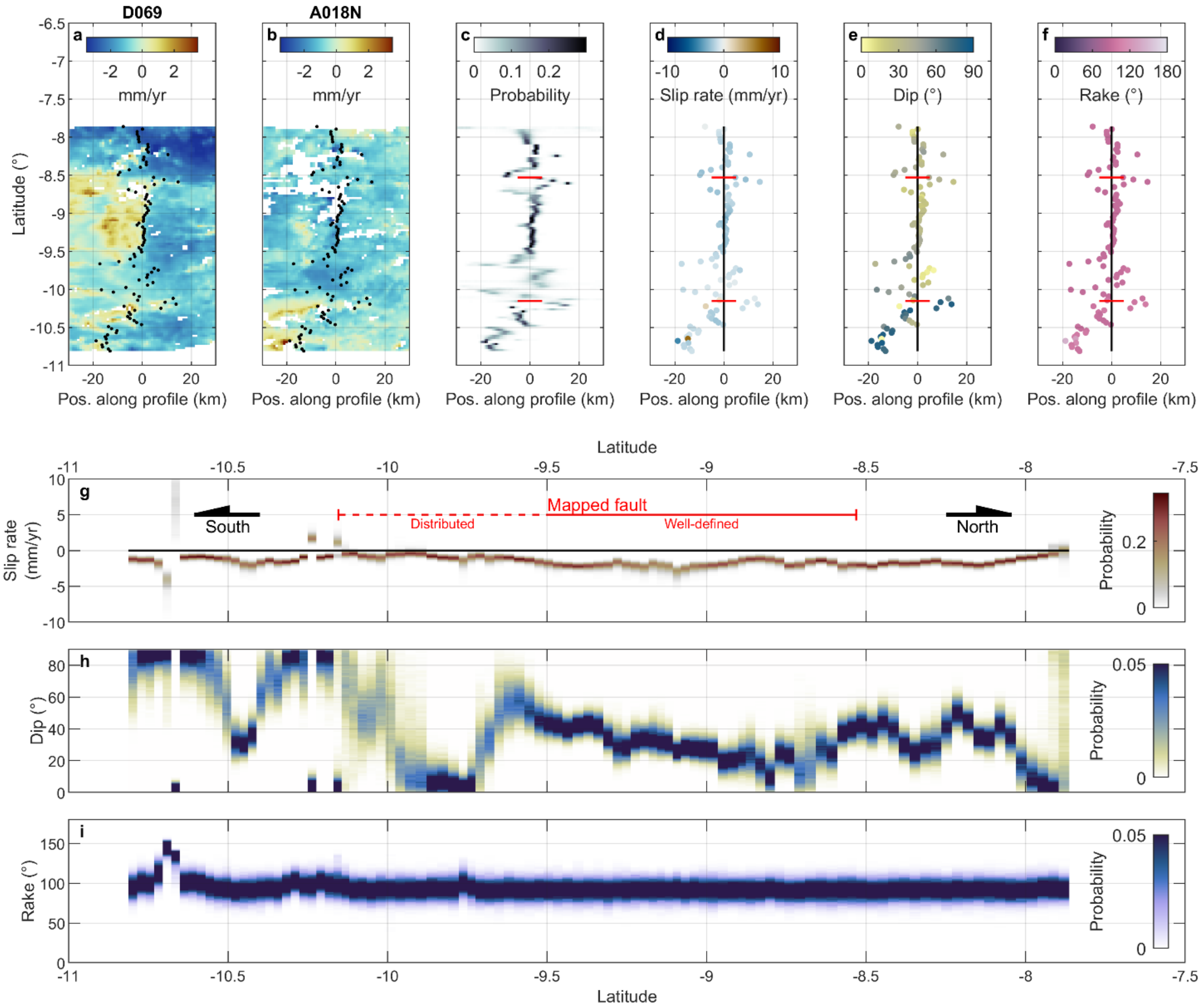

Figure 4: Same as Fig. 2 but with the fault mechanism constrained to be nearly purely normal. The rake is prescribed using the Gaussian prior, $\mathcal{N}(90°,10°)$, corresponding to a mean of 90° and a standard deviation of 10°.

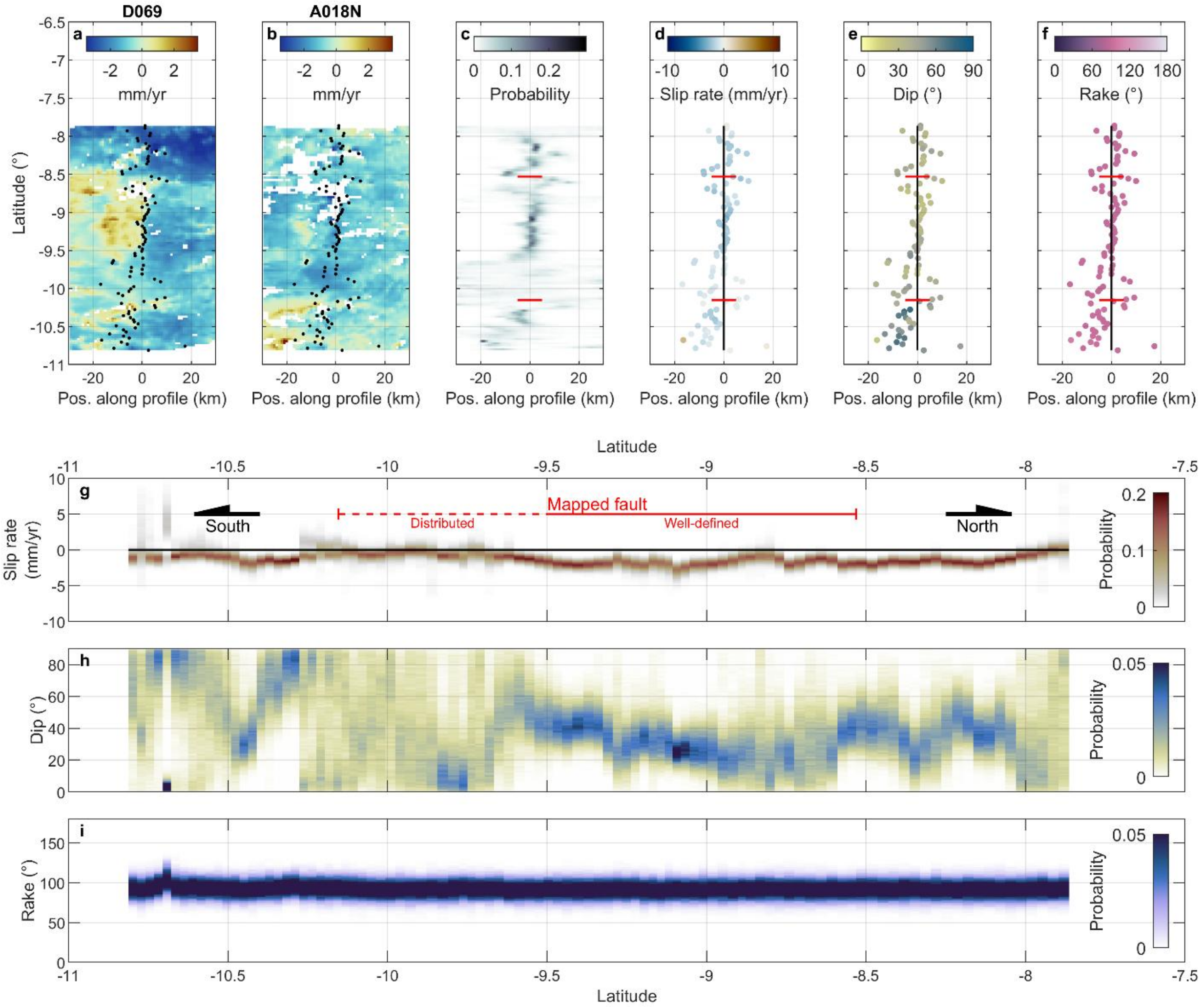

Figure 5: Same as Fig. 4 but using observational uncertainties that are twice as large.

6. Conclusion

Based on InSAR data acquired from 2015 to 2021 and analyzed using a Bayesian framework, this study provides the first geodetic characterization of the kinematics of the CBNF, together with a quantitative assessment of associated uncertainties. Using geodetic observations alone, we infer a slip rate of ∼2-2.5 mm/yr along the well-defined, previously mapped fault trace. This estimate is consistent with independent geological slip rate estimates (Bonnot, 1984; Giovanni, 2007; Hodson, 2013; Margirier et al., 2016; Schwartz, 1988; Siame et al., 2006). However, the noise level of the data do not allow robust constraints on fault rake and dip of the fault when these parameters are left unconstrained. When a purely dip-slip mechanism is imposed, consistent with geological observations, both the slip rate and dip become more tightly constrained. Under this assumption, the dip appears to decrease from ∼45° in the south to ∼20° in the north along the well-defined fault segment. The characteristics inferred for the remaining sections of the fault should be interpreted with caution. Their reliability is limited by several factors, including the presence of diffuse deformation that is not adequately captured by our simplified dislocation model, residual noise in the InSAR data, and the scarcity of independent geological constraints to further restrict the inversion.

Given the ~150 km length of the fault, the nearby population centers, and the history of past catastrophic events in the region, assessing whether parts of the fault are currently locked and accumulating slip deficit is of primary importance. However, the relatively large data uncertainty (~0.74 mm/yr), compared to the inferred loading rate (~2 mm/yr), makes it difficult at present to resolve such behavior with confidence. Extending the InSAR time series, increasing the density of GNSS measurements — which are currently sparse — and analyzing the full temporal evolution of deformation rather than only the mean velocity field would likely improve our ability to evaluate of the seismogenic potential of the CBNF.

References

Bellier, O., Dumont, J. F., Sebrier, M., & Mercier, J. L. (1991). Geological constraints on the kinematics and fault-plane solution of the quiches fault zone reactivated during the 10 November 1946 Ancash earthquake, northern Peru. *Bulletin - Seismological Society of America*, *81*(2), 468–490. https://doi.org/https://doi.org/10.1785/BSSA0810020468

Bonnot, D. (1984). *Neotectonique et tectonique active de la Cordillere Blanche et du Callejon de Huaylas (Andes nord-peruviennes)* [Thèse pour obtenir le grade de docteur]. Université de Paris-Sud.

Cluff, L. S. (1971). Peru earthquake of May 31, 1970; engineering geology observations. *Bulletin of the Seismological Society of America*, *61*(3), 511–533. https://doi.org/10.1785/BSSA0610030511

Cobbing, E. J., Pitcher, W. S., Wilson, J. J., Baldock, J. W., Taylor, W. P., McCourt, W. J., & Snelling, N. J. (1981). *Estudio geológico de la Cordillera Occidental del Norte del Perú - Boletín, Serie D: Estudios Regionales; n° 10*.

Costa, C., Alvarado, A., Audemard, F., Audin, L., Benavente, C., Bezerra, F. H., Cembrano, J., González, G., López, M., Minaya, E., Santibañez, I., Garcia, J., Arcila, M., Pagani, M., Pérez, I., Delgado, F., Paolini, M., & Garro, H. (2020). Hazardous faults of South America; compilation and overview. *Journal of South American Earth Sciences*, *104*(August), 102837. https://doi.org/10.1016/j.jsames.2020.102837

Costa, C., García, J., Alvarado, A., Audemard, F., Benavente, C., Cembrano, J., Delgado, F., González, G., López, M., Minaya, E., Pagani, M., Paolini, M., Pérez, I., & Santibañez, I. (2016, November). The contribution of Neotectonics to Seismic Hazard: Current status and perspectives in South America. *Presentation at the 1st Simp. South American Tectonics*. https://doi.org/https://doi.org/10.13140/RG.2.2.34256.10249

Deverchère, J., Dorbath, C., & Dorbath, L. (1989). Extension related to a high topography: results from a microearthquake survey in the Andes of Peru and tectonic implications. *Geophysical Journal International*, *98*(2), 281–292. https://doi.org/10.1111/j.1365-246X.1989.tb03352.x

Doin, M.-P., Lodge, F., Guillaso, S., Jolivet, R., Lasserre, C., Ducret, G., Grandin, R., Pathier, E., Pinel, V., & Guillaso, S. (2011). *Presentation of the small baseline NSBAS processing chain on a case example:*

The Etna deformation monitoring from 2003 to 2010 using ENVISAT data. http://www.openchannelsoftware.com/projects/ROI

Doser, D. I. (1987). The Ancash, Peru, earthquake of 1946 November 10: evidence for low-angle normal faulting in the high Andes of northern Peru. *Geophysical Journal International*, *91*(1), 57–71. https://doi.org/10.1111/j.1365-246X.1987.tb05213.x

FormaTerre. (2020). FLATSIM data products: Data products generated by FLATSIM (FormaTerre LArge-scale multi-temporal Sentinel-1 InterferoMetry). In *CNES*. https://doi.org/https://doi.org/10.24400/253171/FLATSIM2020

Giovanni, M. K. (2007). *Tectonic and thermal evolution of the Cordillera Blanca detachment system, Peruvian Andes: Implications for normal faulting in a contractional orogen* [Ph.D. dissertation]. University of California.

Grandin, R. (2015, May 1). Interferometric Processing of SLC Sentinel-1 TOPS Data. *Proceedings of Fringe 2015: Advances in the Science and Applications of SAR Interferometry and Sentinel-1 InSAR Workshop*. https://doi.org/10.5270/Fringe2015.pp116

Hasting, W. K. (1970). Monte Carlo sampling methods using Markov chains and their applications. *Biometrica*, *57*, 97.

Hodson, K. (2013). *Morphology, exhumation, and Holocene erosion rates from a tropical glaciated mountain range: the Cordillera Blanca Peru* [Masters of science]. McGill University .

Jolivet, R., Grandin, R., Lasserre, C., Doin, M.-P., & Peltzer, G. (2011). Systematic InSAR tropospheric phase delay corrections from global meteorological reanalysis data. *Geophysical Research Letters*, *38*(17), n/a-n/a. https://doi.org/10.1029/2011GL048757

Klimeš, J., Kilnar, J., Kopačková-Strnadová, V., Pánek, T., McColl, S., & Jelének, J. (2025). Landslides in the glaciated mountains of the Cordillera Blanca, Peru—types, spatial distribution, and conditioning factors. *Landslides*, *22*(3), 803–819. https://doi.org/10.1007/s10346-024-02387-6

Lemrabet, L., Doin, M. P., Lasserre, C., & Durand, P. (2023). Referencing of Continental-Scale InSAR-Derived Velocity Fields: Case Study of the Eastern Tibetan Plateau. *Journal of Geophysical Research: Solid Earth*, *128*(7). https://doi.org/10.1029/2022JB026251

Margirier, A., Audin, L., Robert, X., Herman, F., Ganne, J., & Schwartz, S. (2016). Time and mode of exhumation of the Cordillera Blanca batholith (Peruvian Andes). *Journal of Geophysical Research: Solid Earth*, *121*(8), 6235–6249. https://doi.org/10.1002/2016JB013055

Margirier, A., Audin, L., Robert, X., Pêcher, A., & Schwartz, S. (2017). Stress field evolution above the Peruvian flat-slab (Cordillera Blanca, northern Peru). *Journal of South American Earth Sciences*, *77*, 58–69. https://doi.org/10.1016/j.jsames.2017.04.015

McNulty, B. A., Farber, D. L., Wallace, G. S., Lopez, R., & Palacios, O. (1998). Role of plate kinematics and plate-slip-vector partitioning in continental magmatic arcs: Evidence from the Cordillera Blanca, Peru. *Geology*, *26*(9), 827. https://doi.org/10.1130/0091-7613(1998)026<0827:ROPKAP>2.3.CO;2

Metropolis, N., Rosenbluth, A. W., Rosenbluth, M. N., Teller, A. H., & Teller, E. (1953). Equation of State Calculations by Fast Computing Machines. *The Journal of Chemical Physics*, *21*(6), 1087–1092. https://doi.org/doi:10.1063/1.1699114

Petford, N., & Atherton, M. P. (1992). Granitoid emplacement and deformation along a major crustal lineament: The Cordillera Blanca, Peru. *Tectonophysics*, *205*(1–3), 171–185. https://doi.org/10.1016/0040-1951(92)90425-6

Schwartz, D. P. (1988). Paleoseismicity and neotectonics of the Cordillera Blanca Fault Zone, northern Peruvian Andes. *Journal of Geophysical Research: Solid Earth*, *93*(B5), 4712–4730. https://doi.org/10.1029/JB093iB05p04712

Siame, L. L., Sébrier, M., Bellier, O., & Bourles, D. (2006). Can cosmic ray exposure dating reveal the normal faulting activity of the Cordillera Blanca Fault, Peru? *Revista de La Asociacion Geologica Argentina*, *61*(4), 536–544.

Thollard, F., Clesse, D., Doin, M.-P., Donadieu, J., Durand, P., Grandin, R., Lasserre, C., Laurent, C., Deschamps-Ostanciaux, E., Pathier, E., Pointal, E., Proy, C., & Specht, B. (2021). FLATSIM: The ForM@Ter LArge-Scale Multi-Temporal Sentinel-1 InterferoMetry Service. *Remote Sensing*, *13*(18), 3734. https://doi.org/10.3390/rs13183734

U.S. Geological Survey. (2017). *Advanced National Seismic System (ANSS) Comprehensive Catalog of Earthquake Events and Products: Various*. https://doi.org/https://doi.org/10.5066/F7MS3QZH